

THÈSE PRÉSENTÉE
POUR OBTENIR LE GRADE DE
DOCTEUR
DE L'UNIVERSITÉ DE BORDEAUX
ECOLE DOCTORALE SCIENCES PHYSIQUES ET DE
L'INGÉNIEUR

LASERS, MATIÈRE, NANOSCIENCES

Par **Maxime Lavaud**

Confined Brownian Motion

Sous la direction de : **Thomas Salez**
Co-direction : **Yacine Amarouchene**

Soutenue le 25 décembre 2019

Membres du jury :

Mme. Aude ALPHA	Directrice de Recherche	Université	Rapporteur
M. Bernard BETA	Directeur de Recherche	Université	Rapporteur
M. Georges GAMMA	Directeur de Recherche	Université	Président
Mme. Dominique DELTA	Chargée de Recherche	Université	Examinatrice
M. Eric EPSILON	Ingénieur de Recherche	Université	Examineur
Mme. Jane DOE	Directrice de Recherche	Université	Directrice
Mme. Simone UNTEL	Ingénieure de Recherche	Université	Invitée

Abstract

Lorem ipsum dolor sit amet, consectetur adipiscing elit. Ut purus elit, vestibulum ut, placerat ac, adipiscing vitae, felis. Curabitur dictum gravida mauris. Nam arcu libero, nonummy eget, consectetur id, vulputate a, magna. Donec vehicula augue eu neque. Pellentesque habitant morbi tristique senectus et netus et malesuada fames ac turpis egestas. Mauris ut leo. Cras viverra metus rhoncus sem. Nulla et lectus vestibulum urna fringilla ultrices. Phasellus eu tellus sit amet tortor gravida placerat. Integer sapien est, iaculis in, pretium quis, viverra ac, nunc. Praesent eget sem vel leo ultrices bibendum. Aenean faucibus. Morbi dolor nulla, malesuada eu, pulvinar at, mollis ac, nulla. Curabitur auctor semper nulla. Donec varius orci eget risus. Duis nibh mi, congue eu, accumsan eleifend, sagittis quis, diam. Duis eget orci sit amet orci dignissim rutrum.

Table of Contents

Abstract	i
Table of Contents	ii
List of Figures	iv
Nomenclature	v
List of Abbreviations	v
1 Introduction	1
2 Brownian motion	3
2.1 The Brownian motion discovery	3
2.2 The Einstein Brownian theory	4
2.3 Stochastic Differential Equations	8
2.4 The confined Brownian motion	12
3 Particle characterization and particle tracking using interference prop- erties	16
3.1 Introduction	16
3.2 In-line holographic video microscopy theory	16
3.2.1 Reflection Interference Contrast Microscopy	16
3.2.2 Lorenz-Mie Fit	19
3.2.3 Rayleigh-Sommerfeld back-propagation	21
3.2.4 Conclusion	25
3.3 Experimental setup	25
3.4 Hologram fitting strategy	25
3.4.1 How to fasten the process ?	25
3.4.2 Radius and optical index characterization	27
References	29

List of Figures

Fig. 1:	Brownian motion of 1 μm particle in water tracked by hand by Jean Perrin and his colleagues, each point are timely space by 30 seconds and 16 divisions represents 50 μm	4
Fig. 2:	Simulation of bulk Brownian motion of 1 μm particles in water. On the top each line represents the trajectory of a Brownian particle over 100 seconds a total of 100 trajectories or shown. On the bottom, bullets represents the MSD computed from the simulated trajectories. The black plain line represents the Einstein's theory, which is computed from the square of Eq.2.2.11.	7
Fig. 3:	Figure extracted from [13], on the left is the experimental setup used. It is an inverted microscope used in order to track particle of size $2R$ inside a cell of thickness t . On the right is their final result, where they measure the diffusion parallel coefficient D_{\perp} given by Eq.2.4.2, here normalized by D_0 the bulk diffusion coefficient as a function of γ a confinement constant $\gamma = (\langle z \rangle - a)/a$	13
Fig. 4:	On the left, plot of the Gibbs-Boltzmann distribution Eq.2.4.10 for $a = 1 \mu\text{m}$, $B = 4$, $\ell_D = 100 \text{ nm}$ and $\Delta\rho = 50 \text{ kg.m}^{-3}$. On the right, local diffusion coefficient normalized by bulk diffusion coefficient $D_0 = k_B T/\gamma$, given by Eq.2.4.2 and Eq.2.4.1	15
Fig. 5:	Figure from [36] representing RISM with two wavelengths. (a) Left: interference patterns created with a wavelength $\lambda_1 = 532 \text{ nm}$ (scale bar 5 μm). Right: radial intensity profile (black dots) extracted from the image, azimuthally averaged (magenta line) and fitted with Eq.3.2.8 to measure the height of the particle (here h). (b) Same as (a) with a wavelength $\lambda_2 = 635 \text{ nm}$. (c) Time series of the height of a particle h (green: λ_1 , magenta: λ_2) and the particle velocity measured along the flow in blue.	17
Fig. 6:	a) Raw hologram of a 2.5 μm polystyrene particle measured experimentally with the setup detailed in the chapter 3.3. b) Background obtained by taking the mean value of the time series of images of the diffusing particle. c) Normalized hologram given by dividing a) by b). d) Result of the fit of c) using Eq.3.2.12 the particle is found to be at a height $z = 14.77\mu\text{m}$. e) Comparison of the normalized radial intensity, obtained experimentally from c) and theoretically from d).	22

- Fig. 7: On the left, experimentally measured holograms' radial intensity stack. Generated from a polystyrene bead (Sigma Aldrich) of nominal radius $a = 1.5 \pm 0.035 \mu\text{m}$ using the experimental setup explained in chapter 3.3. The calibration of this particle radius and optical index is shown in Fig.11. On the right, the corresponding theoretical stack using the result of each individual hologram's fit. 23
- Fig. 8: Figure from [57] a) Volumetric reconstruction using Eq.3.2.21 of the scattered intensity due to a single colloidal sphere, colored by intensity. b) Volumetric reconstructions of 22 individual $1.58 \mu\text{m}$ diameter silica spheres organised in bcc lattice using holographic optical tweezers in distilled water. Colored regions indicate the isosurface of the brightest 1 percent of reconstructed voxels. 24
- Fig. 9: Photo of the custom build microscope used along my thesis. It is mainly composed of Thorlabs cage system. The camera used is a Basler acA1920-155um, we use a x60 magnification and 1.30 numerical aperture oil immersion objective and the laser is colimated and has a $521 \mu\text{m}$ wavelength. 26
- Fig. 10: Schematic of the experimental setup. A laser plane wave of intensity E_0 illuminates the chamber containing a dilute suspension of microspheres in water. The light scattered by a particle interferes with the incident beam onto the focal plane of an objective lens, that magnifies the interference pattern and relays it to a camera. 27
- Fig. 11: 2D Probability density function of the measurements of the optical index n_p and radius a . Black lines indicate iso-probability. Taking the 10% top probability, we measure $n_p = 1.585 \pm 0.002$ and $a = 1.514 \pm 0.003 \mu\text{m}$. 28

1 Introduction

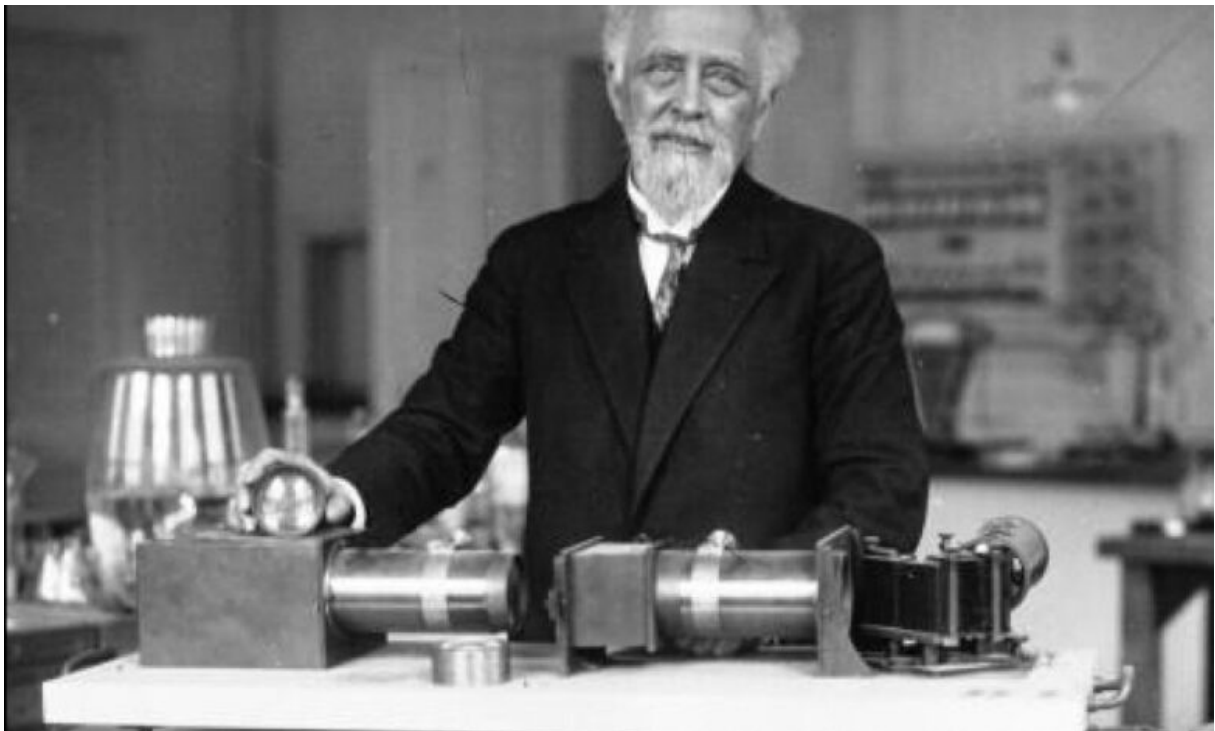
Since the observations of Gordon Moore in the 60's we know that the technological progress is bound to our ability to miniaturize. It's indeed due to the miniaturization that we are able to have more computational power leading to the rise of new technologies like the Deep Learning [1] that showed the need of large computational capabilities by having the computer program *AlphaGo* beating *Lee Sedol* one of the greatest player of *Go* in 2016. Since this powerful demonstration AIs using the same technologies are showing up in every field, from the language translator to autonomous cars and is now starting to be extensively used in physics with in 2020 the first focus session on machine learning at the *March Meeting* that continued this year with presentations at every sessions. The success of Deep learning is not due to the fact that it's new and fancy algorithm since it known for several decade but only the fact that the miniaturization permitted to do the stunning amount of computation needed to have a smart AI. Our ability to use this technologies is finally bound to our ability to understand the surface physics at the nanometer scale.

On another side we have microfluidic since the 80s which is an incredible multidisciplinary field involving chemistry, engineering, soft matter physics and also biotechnology. Microfluidic permitted the development of daily life technologies like the ink-jet printers or more advanced tools such as DNA chips [2] or lab-on-a-chip technology [3]. The ability to compose with a lot of different system to build microfluidic systems is a wonderful playground for physicists which gave a lot of complex systems in confinement to study and understand how different boundaries can change the dynamic properties of a system. At a time of miniaturization and nanotechnologies, the need of tools permitting the systematic study of complex confined system is a key.

In order to address these challenges my work in the past three years focused on using the confined Brownian motion. Brownian Motion is a central paradigm in modern science. It has implications in fundamental physics, biology, and even finance, to name a few. By understanding that the apparent erratic motion of colloids is a direct consequence of the thermal motion of surrounding fluid molecules, pioneers like Einstein and Perrin provided decisive evidence for the existence of atoms [4, 5]. Specifically, free Brownian motion in the bulk is characterized by a typical spatial extent evolving as the square root of time, as well as Gaussian displacements. At a time of miniaturization and interfacial science, and moving beyond the idealized bulk picture, it is relevant to consider the added roles of boundaries to the above context. Indeed, Brownian motion at interfaces and in confinement is a widespread practical situation in microbiology and nanofluidics. In such case, surface effects become dominant and alter drastically the Brownian statistics, with key

implications towards: i) the understanding and smart control of the interfacial dynamics of microscale entities; and ii) high-resolution measurements of surface forces at equilibrium. Interestingly, a confined colloid will exhibit non-Gaussian statistics in displacements, due to the presence of multiplicative noises induced by the hindered mobility near the wall [6–8]. Besides, the particle can be subjected to electrostatic or Van der Waals forces [9] exerted by the interface, and might experience slippage too [10, 11]. Considering the two-body problem, the nearby boundary can also induce some effective interaction [12]. Previous studies have designed novel methods to measure the diffusion coefficient of confined colloids [13–18], or to infer surface forces [19–24].

In the the first part of the manuscript I will present the history of the Brownian motion and it's basic theory. In a second part I will present particle tracking using Mie holography and our experimental setup. Then the third part will focus on one trajectory analysis in order to infer the surface induced effects on the Brownian motion. In a last chapter I will present more complex inference.



2 Brownian motion

2.1 The Brownian motion discovery

In 1827 the Scottish botanist Robert Brown published a paper [25] on his observation on the pollen of *Clarkia pulchella* with a lot of details on his taught processes. His experiments were made to understand the flower reproduction, but, as he was looking through the microscope he observed some minute particles ejected from the pollen grains. At first, he thought this movement was a test to find the male organ, then looking at grains Mosses and *Equiseta* which had been dried up for one hundred years, he was surprised to see this "peculiar" movement and since he was able to increase the number of particle by bruising ovule or seeds of *Equisetum* he abandoned his supposition. Interestingly each time that he encountered a material that he was able to reduce to a fine enough powder to be suspended in water, he observed a constant motion, although, he never guessed the origin of the particle's movement.

The difficulty at this time to observe and capture this movement made the study of what we call today Brownian motion quite difficult and the first theoretical work on erratic movement was actually done by Louis Bachelier in his PhD thesis "The theory of speculation", where he describes a stochastic analysis of the stock and option market. The mathematical description is still a used in the modern development of tools for the economic industry.

It's finally in 1905 that Albert Einstein describe that "bodies of microscopically visible size suspended in a liquid will perform movements of such a magnitude that they can be easily observed in a microscope" [4]. A nice remark to make here is that in 1948 Einstein wrote a letter to one of his friend where he stated having deduced the Brownian motion "from mechanics, without knowing that anyone had already observed anything of the kind" [26].

It's in 1908 that Jean Perrin published his experimental work on the Brownian motion, that way he was able to measure the Avogadro number and prove the kinetic theory that Einstein developed. I would also cite M. Chaudesaigues and M. Dabrowski, who helped J. Perrin to track the particles by hand, half-minutes by half-minutes, for more than 3000 displacements (25 hours) and several particles. This impressive and daunting work is highly detailed in "*Mouvement brownien et molécules*" [27]. This is partly due to this work than J. Perrin received the Nobel award in 1926.

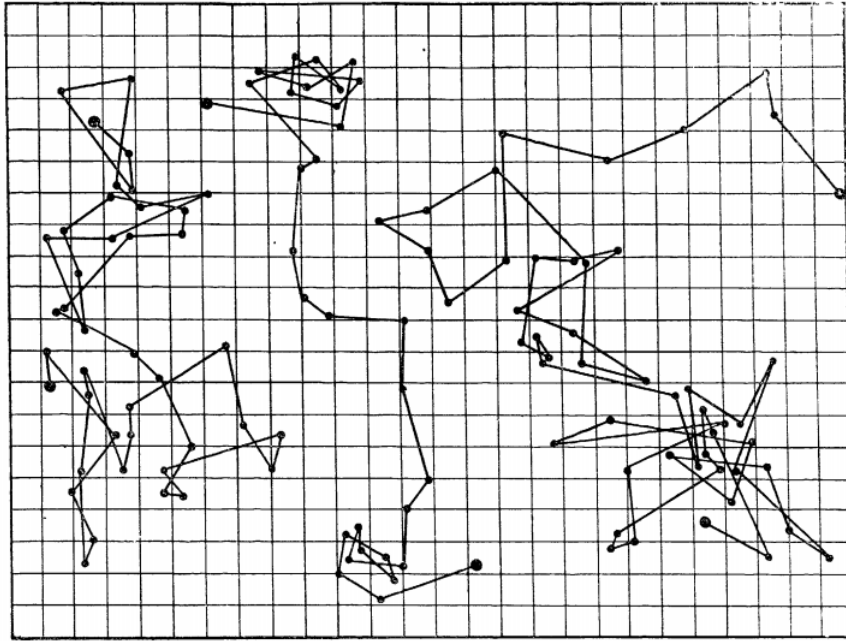


Figure 1: Brownian motion of $1 \mu\text{m}$ particle in water tracked by hand by Jean Perrin and his colleagues, each point are timely space by 30 seconds and 16 divisions represents $50 \mu\text{m}$

2.2 The Einstein Brownian theory

In this section we will derive the main characteristic of the bulk Brownian motion in the manner of Einstein in 1905 by summarizing the section 4 of [4]. We will then examine the random motion of particles suspended in a liquid and their relation to diffusion, caused by thermal molecular motion. We assume that each particle motion is independent of other particles; also the motion of one particle at different time interval as to be taken independent process as long as the time interval is not too small. We now introduce a time interval τ which as to be small compared to the observation time but small enough so that the displacement between two consecutive time intervals τ may be taken as independent events (i.e. the over damped regime).

For simplicity, we will here look only at the Brownian motion of n particles in 1D along the x axis. In a time interval τ the position of each individual particle will increase by a displacement Δ , positive or negative and different for all the particles. The number of particle dn experiencing a displacement lying between Δ and $\Delta + d\Delta$ in a time interval τ is written as:

$$dn = n\varphi(\Delta)d\Delta, \quad (2.2.1)$$

where

$$\int_{-\infty}^{\infty} \varphi(\Delta) d\Delta = 1, \quad (2.2.2)$$

and φ is nonzero only for very small displacement Δ and satisfies $\varphi(\Delta) = \varphi(-\Delta)$.

Let $f(x, t)$ be the number of particles per unit volume. From the definition of the function $\varphi(\Delta)$ we can obtain the distribution of particles found at time $t + \tau$ from their distribution at a time t , we obtain:

$$f(x, t + \tau) dx = dx \int_{\Delta=-\infty}^{\Delta=+\infty} f(x + \Delta, t) \varphi(\Delta) d\Delta. \quad (2.2.3)$$

Since τ is very small, we have:

$$f(x, t + \tau) = f(x, t) + \tau \frac{\partial f}{\partial t}. \quad (2.2.4)$$

On the other side we can Taylor expand $f(x + \Delta, t)$ in powers of Δ since only small values of Δ contribute. We obtain:

$$f(x + \Delta, t) = f(x, t) + \Delta \frac{\partial f(x, t)}{\partial x} + \frac{\Delta^2}{2!} \frac{\partial^2 f(x, t)}{\partial x^2} \dots \quad (2.2.5)$$

Putting all together, in Eq.2.2.3 we obtain:

$$f + \frac{\partial f}{\partial t} \tau = f \int_{-\infty}^{+\infty} \varphi(\Delta) d\Delta + \frac{\partial f}{\partial x} \int_{-\infty}^{+\infty} \Delta \varphi(\Delta) d\Delta + \frac{\partial^2 f}{\partial x^2} \int_{-\infty}^{+\infty} \frac{\Delta^2}{2} \varphi(\Delta) d\Delta \dots \quad (2.2.6)$$

On the right-hand side, since $\varphi(x) = \varphi(-x)$ all even terms will vanish and all the odd terms will be very small compared to the precedent. If we take into account 2.2.2 and only the first and third term of the right-hand side, by putting:

$$\frac{1}{\tau} \int_{-\infty}^{+\infty} \frac{\Delta^2}{2} \varphi(\Delta) d\Delta = D, \quad (2.2.7)$$

the Eq.2.2.6 finally becomes:

$$\frac{\partial f}{\partial t} = D \frac{\partial^2 f}{\partial x^2}. \quad (2.2.8)$$

We can here recognize a differential equation for the diffusion with D the diffusion coefficient. We will now initiate the same position $x = 0$ for all the particle at $t = 0$ as in the Fig.2 and $f(x, t)dx$ now denoting the number of particles whose position as increased between the times $t = 0$ and $t = t$ by a quantity lying between x and $x + dx$ such that we must have:

$$f(x \neq 0, t = 0) = 0 \text{ and } \int_{-\infty}^{+\infty} f(x, t)dx = n. \quad (2.2.9)$$

The solution of this equation is known and the same as the heat equation and is given by the Gaussian:

$$f(x, t) = \frac{1}{\sqrt{4\pi D}} \frac{\exp \frac{-x^2}{4Dt}}{\sqrt{t}}. \quad (2.2.10)$$

From this solution we can see that the mean value of the displacement of all the particles along the x axis is equal to 0 and the square root of the arithmetic mean of the squares of displacements (that we commonly call Mean Square displacement (MSD)) is given by:

$$\lambda_x = \sqrt{2Dt}. \quad (2.2.11)$$

The mean displacement is thus proportional to the square root of time, this result is generally the first behavior that we check when we study for the first time experimental Brownian motion. We can further suppose that in 3D, the square root of the MSD will be given by $\lambda_x \sqrt{3}$

Previously in his paper, in the chapter 3, he had found by writing the thermodynamic equilibrium of a suspension of particles that the diffusion coefficient of a particle should be written:

$$D = \frac{RT}{N_A} \frac{1}{6\pi\eta a}, \quad (2.2.12)$$

with R the gas constant, T the temperature, N_A the Avogadro number and η the fluid viscosity. Thus, an experimental observation measurement could lead to a measurement of the Avogadro number and the true size of the atoms since:

$$N_A = \frac{t}{\lambda_x^2} \frac{RT}{3\pi\eta a}. \quad (2.2.13)$$

Finally, he ends up in paper [4] by saying *"Let us hope that a researcher will soon succeed in solving the problem posed here, which is of such importance in the theory of heat!"*. I'd like here to emphasize on the importance of solving this problem in very beginning of the 19's. At this time two theory about the fundamental matter components existed, one's seeing only energy and a second one, atoms, especially supported by Boltzmann and his kinetic theory of gases, here used by Einstein. Thus, an experimental proof of Eq.2.2.12 would prove the existence of atoms and molecules. Due to a lot of theoretical misunderstanding of the theory and experimental error scientist such as Svedberg or Henri thought that Einstein's theory was false [28] by even proving that the statistical properties of the Brownian motion was changing with the pH of the solution. It's finally in 1908 that Chaudesaigues and Perrin published all the evidence to prove Einstein's theory mainly by their ability to create particle emulsion of well controlled radius.

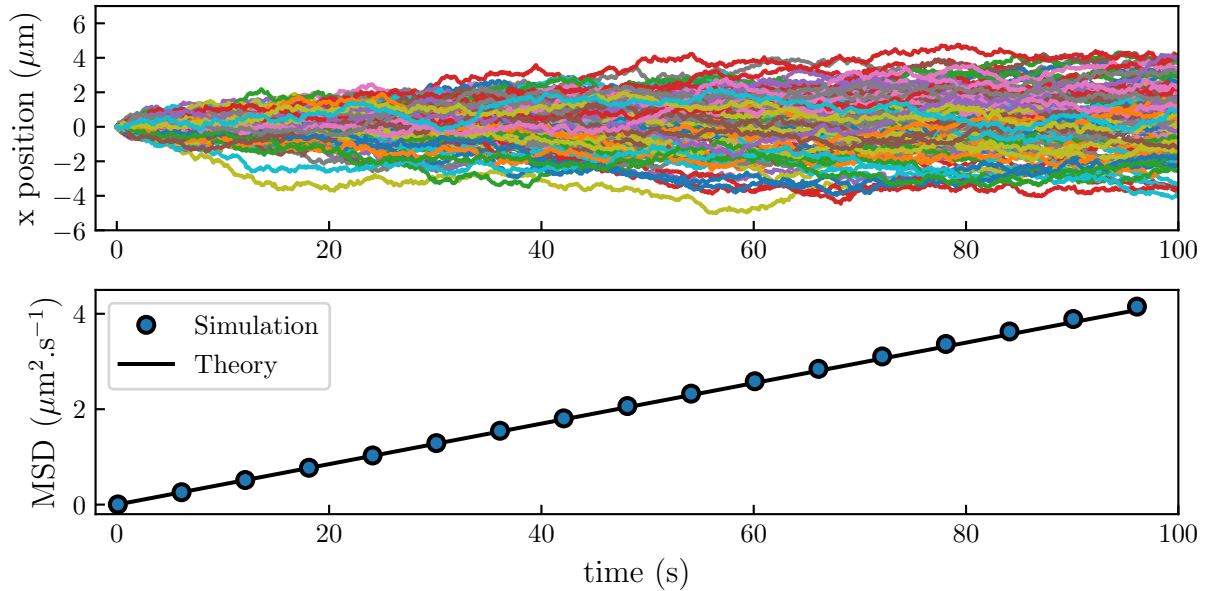


Figure 2: Simulation of bulk Brownian motion of $1 \mu\text{m}$ particles in water. On the top each line represents the trajectory of a Brownian particle over 100 seconds a total of 100 trajectories or shown. On the bottom, bullets represents the MSD computed from the simulated trajectories. The black plain line represents the Einstein's theory, which is computed from the square of Eq.2.2.11.

2.3 Stochastic Differential Equations

In physics we generally write Brownian motion with Stochastic Differential Equations (SDE). This model was introduced in 1908 by Langevin [29], since it benefits of a correct mathematical definition of the noise, this model is now used by the major part of physicists working on random processes. Note than it can also be found under the name of Langevin equation. This model is write as follows:

$$mdV_t = -\gamma V_t dt + \alpha dB_t, \quad (2.3.1)$$

with m the mass and V_t the velocity of the particle. This SDE is finally the Newton's second law, relating the particle momentum changes on the left-hand side of the equation and an external force on the right-hand side. We see that the external force applied on the particle is given by two terms: a friction term, with a friction coefficient γ plus a random force with a a coefficient that we will detail for a spherical particle and dB_t is a random noise which has a Gaussian distribution of zero mean thus:

$$\langle dB_t \rangle = 0, \quad (2.3.2)$$

and we chose de variance to be equal to dt giving :

$$\langle dB_t^2 \rangle = dt. \quad (2.3.3)$$

For a spherical particle the friction term is given by the Stoke's formula: $\gamma = 6\pi\eta a$ with η the fluid viscosity and a the particle radius. Thus, we can derive the mean value of the particle velocity as:

$$\langle dV_t \rangle = -\frac{\gamma}{m} \langle V_t \rangle + \frac{\alpha}{m} \langle dB_t \rangle, \quad (2.3.4)$$

with the properties of dB_t given by Eq.2.3.2, it becomes:

$$\langle dV_t \rangle = -\frac{\gamma}{m} \langle V_t \rangle, \quad (2.3.5)$$

which as a familiar solution:

$$\langle V_t(t) \rangle = V_0 e^{-\frac{\gamma}{m}t}. \quad (2.3.6)$$

This result shows that the average of the velocity should decay to zero with a characteristic time $\tau_B = \frac{m}{\gamma}$ for the polystyrene particle used during my experiments which are micrometric we have $\tau_B \approx 10^{-7}$ s. This means that if we measure the displacement of a particle with a time interval $\Delta t \gg \tau_B$ the displacement can be taken as independent events as it was stated by Einstein. In physics terms, this means that we are in the over damped regime and $dV_t = 0$ thus leading to the over-damped Langevin equation :

$$-\gamma V_t + \alpha dB_t = 0. \quad (2.3.7)$$

The experiments done during my thesis used a video camera that can reach a maximum of hundreds frames per second (fps) reaching time steps of $\approx 10^{-2}$ s. Therefore, all my work falls into the over damped regime. Before dropping the full expression of the Langevin we can use it to compute how $\langle V_t^2 \rangle$ using Taylor expansion we have:

$$\begin{aligned} dV_t^2 &= \frac{\partial V_t^2}{\partial V_t} dV_t + \frac{1}{2} \frac{\partial^2 V_t^2}{\partial V_t^2} dV_t^2 \\ &= 2V_t dV_t + \frac{1}{2} 2dV_t^2 \\ &= 2V_t \left(-\frac{\gamma}{m} V_t dt + \frac{\alpha}{m} dB_t \right) + \frac{\alpha^2}{m^2} dB_t^2 + o(dt^2). \end{aligned} \quad (2.3.8)$$

Taking the average then gives:

$$\langle dV_t^2 \rangle = \left[2\frac{\gamma}{m} \langle V_t^2 \rangle + \frac{\alpha^2}{m^2} \right] dt. \quad (2.3.9)$$

Since equilibrium average in thermodynamic must become time independent, we have:

$$\langle V_t^2 \rangle = \frac{\alpha^2}{2\gamma m}. \quad (2.3.10)$$

However, from the equipartition of energy we also know that:

$$\langle \frac{1}{2}mV_t^2 \rangle = \frac{1}{2}k_B T, \quad (2.3.11)$$

this equation permits a direct determination of the amplitude of the noise α :

$$\alpha = \sqrt{2k_B T \gamma}. \quad (2.3.12)$$

Using this model, the position of the particle is given by the integration of V_t such as the position at a time t is given by

$$X_t = \int_0^t V_{t'} dt'. \quad (2.3.13)$$

the MSD is then written as:

$$\langle X_t^2 \rangle = \int_0^t \int_0^t \langle V_{t'} V_{t''} \rangle dt' dt''. \quad (2.3.14)$$

We need to derive the correlation function of the velocity $\langle V_{t'} V_{t''} \rangle$ using Eq.2.3.6 we can write:

$$\langle V_t V_0 \rangle = \langle V_0^2 \rangle e^{-t/\tau_B}. \quad (2.3.15)$$

As the equilibrium state is invariant with a time translation and assume that V_0 as an equilibrium steady state distribution such as $\langle V_0^2 \rangle = k_B T/m$ we have:

$$\langle V_t V_{t'} \rangle = \frac{k_B T}{m} e^{-|t-t'|/\tau_B}. \quad (2.3.16)$$

By using the symmetry of the absolute function we can solve Eq.2.3.14 by splitting the integral where $t' > t''$ and where $t' < t''$:

$$\begin{aligned}
\langle X_t^2 \rangle &= 2 \frac{k_B T}{\gamma} = \int_0^t dt' \int_0^{t'} dt'' e^{-|t'-t''|/\tau_B} = 2 \frac{k_B T}{\gamma} \left(\int_0^t dt' [1 - e^{-t'/\tau_B}] \right) \\
&= 2 \frac{k_B T}{\gamma} (t - \tau_B [1 - e^{-t/\tau_B}]),
\end{aligned} \tag{2.3.17}$$

we can extract two results from that equation, at short time $t \ll \tau_B$

$$\begin{aligned}
\langle X_t^2 \rangle &= 2 \frac{k_B T}{\gamma} \left(t - \tau_B \left[1 - 1 - \frac{t}{\tau_B} + \frac{t^2}{2\tau_B^2} \right] \right) \\
&= \frac{k_B T}{m} t^2.
\end{aligned} \tag{2.3.18}$$

This is the ballistic regime, if one can experimentally explore time shorter than τ_B he will then measure the real velocity of the particle and observe that it has the Maxwell-Boltzmann distribution. At longer time, $t \gg \tau_B$ the MSD is given by:

$$\langle X_t^2 \rangle = 2 \frac{k_B T}{\gamma} t. \tag{2.3.19}$$

This is the Brownian regime where the MSD is linear with the time as depicted by Einstein, and we identify the diffusion coefficient of the particle $D = k_B T / \gamma$ which is commonly called the Stokes-Einstein relation. It is possible to simulate an over damped bulk Brownian trajectory by simply replacing in Eq.2.3.7 $\langle V_t \rangle$ by $(x_i - x_{i-1}) / \Delta t$ thus giving:

$$x_i = x_{i-1} + \sqrt{2D} w_i, \tag{2.3.20}$$

with w_i a Gaussian distributed random number generated with a mean $\langle w_i \rangle = 0$ and a standard deviation $\langle w_i^2 \rangle = dt$, a trajectory of N points can be simulated with a few lines of python as in the following snippet code which was used to create Fig.2.

```

import numpy as np
N = 1000 # trajectory length
D = 1 # diffusion coefficient
dt = 0.5 # time step
trajectory = np.cumsum(np.sqrt(2*D)*np.random.normal(0, np.sqrt(dt), N))

```

2.4 The confined Brownian motion

We have seen that the bulk Brownian motion is well known and documented for a long time. But, in the real world, the boundaries are not at infinity and could play a role in the process of diffusion. Indeed, it was theorized by H. Faxen [30] that the presence of a wall would change the Stokes-Einstein relation with a viscosity dependent to the position of the particle. As the particle get closer to a surface, the presence of the non-slip boundary condition make the fluid harder to push, thus increasing the local viscosity of the particle. This variation of the viscosity will be different for orthogonal and parallel displacement to the wall, thus we write respectively η_{\perp} and η_{\parallel} with η_0 being the fluid viscosity and z the height of the particle:

$$\eta_{\perp} = \frac{4}{3}\eta_0 \sinh \beta \sum_{n=1}^{\infty} \frac{n(n+1)}{2n-12n+3} \left[\frac{2\sinh(2n+1)\beta + (2n+1)\sinh 2\beta}{4\sinh^2(n+1/2)\beta - (2n+1)^2\sinh^2\beta} - 1 \right], \quad (2.4.1)$$

and

$$\eta_{\parallel} = \eta_0 \left[1 - \frac{9}{16}\xi + \frac{1}{8}\xi^3 - \frac{45}{256}\xi^4 - \frac{1}{16}\xi^5 \right]^{-1}, \quad (2.4.2)$$

where $\xi = \frac{a}{z+a}$ and $\beta = \cosh^{-1}(\xi)$. It is possible to simplify the form of η_{\perp} by using a Padé approximation, which is correct up to 1% of accuracy:

$$\eta_{\perp} = \eta_0 \frac{6z^2 + 9az + 2a^2}{6z^2 + 2az}. \quad (2.4.3)$$

Of course, this local viscosity is directly reflected on the diffusive properties of the particle, hence a local diffusion coefficient, which we write:

$$D_i(z) = \frac{k_B T}{6\pi\eta_i(z)a}. \quad (2.4.4)$$

One of the first experimental measurement of the local diffusion coefficient was brought by Faucheux and Libchaber [13] where they measured the mean diffusion coefficient with various gaps and particle radius their results can be found in the Fig.3.

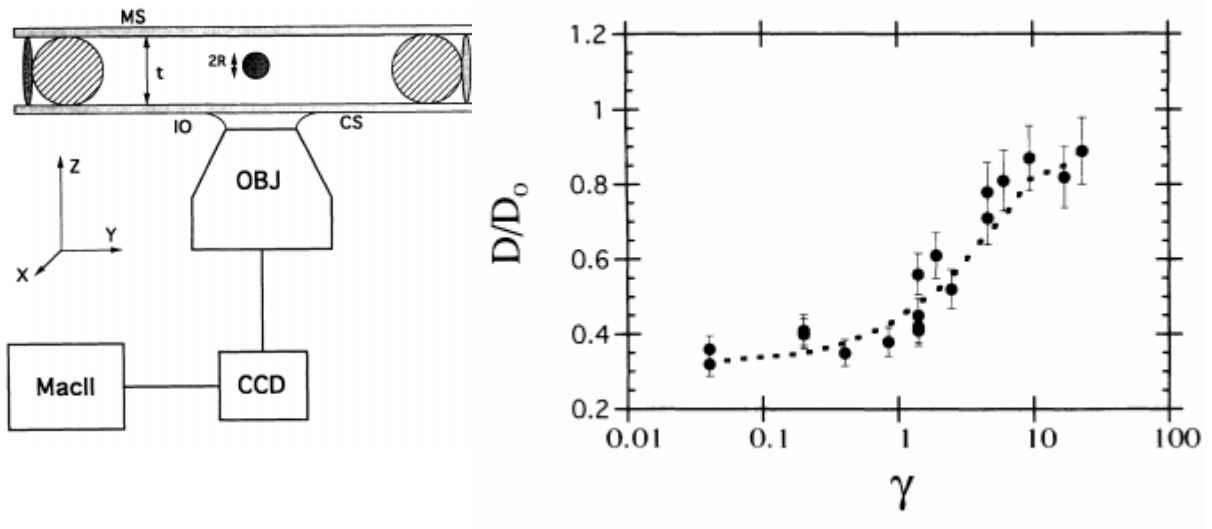


Figure 3: Figure extracted from [13], on the left is the experimental setup used. It is an inverted microscope used in order to track particle of size $2R$ inside a cell of thickness t . On the right is their final result, where they measure the diffusion parallel coefficient D_{\perp} given by Eq.2.4.2, here normalized by D_0 the bulk diffusion coefficient as a function of γ a confinement constant $\gamma = (\langle z \rangle - a)/a$.

Another interesting physical aspect to take into account when looking at confined Brownian motion is the potential the particle is lying into. Let's first consider the weight of the particle. Indeed, if the particle density does not match the fluid's one, a spherical particle will lie in a gravity potential given by:

$$U_g(z) = \frac{4}{3}\pi a^3(\rho_P - \rho_F)gz, \quad (2.4.5)$$

that we can rewrite for simplicity

$$\frac{U_g(z)}{k_B T} = \frac{z}{\ell_B}, \quad (2.4.6)$$

with ℓ_B the Boltzmann length which represents the balance between the kinetic energy and the weight of the particle:

$$\ell_B = \frac{k_B T}{\frac{4}{3}\pi a^3 \Delta \rho g}. \quad (2.4.7)$$

Let's now consider the interactions with the substrate, glass slides when immersed in water do charge negatively as well as polystyrene particles that we use. We will then have repulsive electrostatic interactions between the wall and the particles, the corresponding potential can be written as [31]:

$$\frac{U_{\text{elec}}(z)}{k_{\text{B}}T} = B e^{-z/\ell_{\text{D}}}, \quad (2.4.8)$$

where B is the amplitude of electrostatic interactions, representing the surface charges and ℓ_{D} being the Debye length, which is the characteristic length of the electrostatic interactions. The particle is thus lying in a total potential given by:

$$\frac{U(z)}{k_{\text{B}}T} = B e^{-z/\ell_{\text{D}}} + \frac{z}{\ell_{\text{B}}}. \quad (2.4.9)$$

From this total potential one can construct the Gibbs-Boltzmann distribution in position:

$$P_{\text{eq}}(z) = A e^{\frac{U}{k_{\text{B}}T}}, \quad (2.4.10)$$

where A is a normalization constant so that $\int P_{\text{eq}} = 1$. This distribution gives us the probability to find the particle at a height z . The exponential decay due to the gravity was first measured by Perrin [5] by methodically counting through a microscope the number of colloids in suspension as a function on the height.

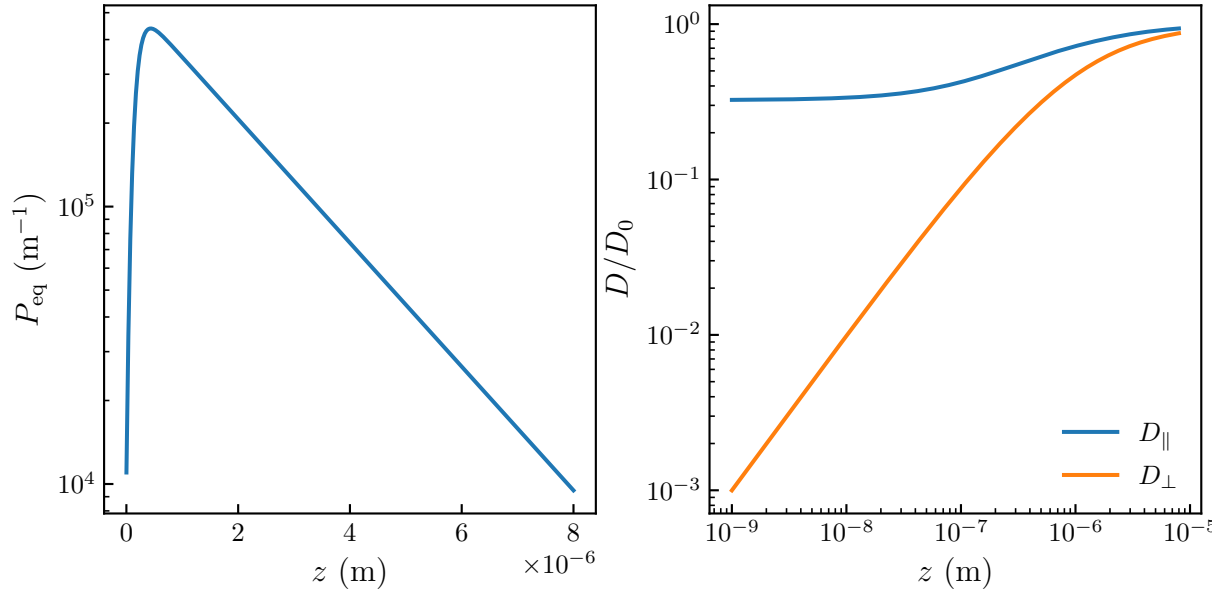


Figure 4: On the left, plot of the Gibbs-Boltzmann distribution Eq.2.4.10 for $a = 1 \mu\text{m}$, $B = 4$, $\ell_D = 100 \text{ nm}$ and $\Delta\rho = 50 \text{ kg.m}^{-3}$. On the right, local diffusion coefficient normalized by bulk diffusion coefficient $D_0 = k_B T / \gamma$, given by Eq.2.4.2 and Eq.2.4.1

3 Particle characterization and particle tracking using interference properties

3.1 Introduction

Properties of coherent light to produce interferences is widely used in metrology for a long time with, for example, the famous Fabry-Pérot [32, 33] and Michelson interferometers [34]. The latter was initially used to measure earth's rotation and is still used today, in particular, for the recent measurement of gravitational waves [35]. Since the beginning of the century, interest on tracking and characterizing colloidal particles risen thanks to the democratization of micro fluidics and lab-on-a-chip technologies. In the following I will provide some insights on the three most used :

- Reflection Interference Contrast Microscopy (RICM)
- Lorenz-Mie fit
- Rayleigh-Sommerfeld back-propagation

The first one, RICM, uses the principle of optical difference path as a Michelson interferometer. The other two, uses the interference between the light scattered by the colloid and the incident light. Generaly, both of the sources thware colinear, wes speak of in-line holography.

3.2 In-line holographic video microscopy theory

3.2.1 Reflection Interference Contrast Microscopy

Reflection Interference Contrast Microscopy was first introduced in cell biology by Curtis to study embryonic chick heart fibroblast [37] in 1964. RICM gained in popularity 40 years after both in biology and physics [38–43]. It was also used recently in soft matter physics to study elastohydrodynamic lift at a soft wall [36].

When we illuminate a colloid with a plane wave from the bottom, a part of the light is reflected at the surface of the glass substrate and at the colloid's surface. The difference of optical path between the the two reflection create interference parterns. Let's take an

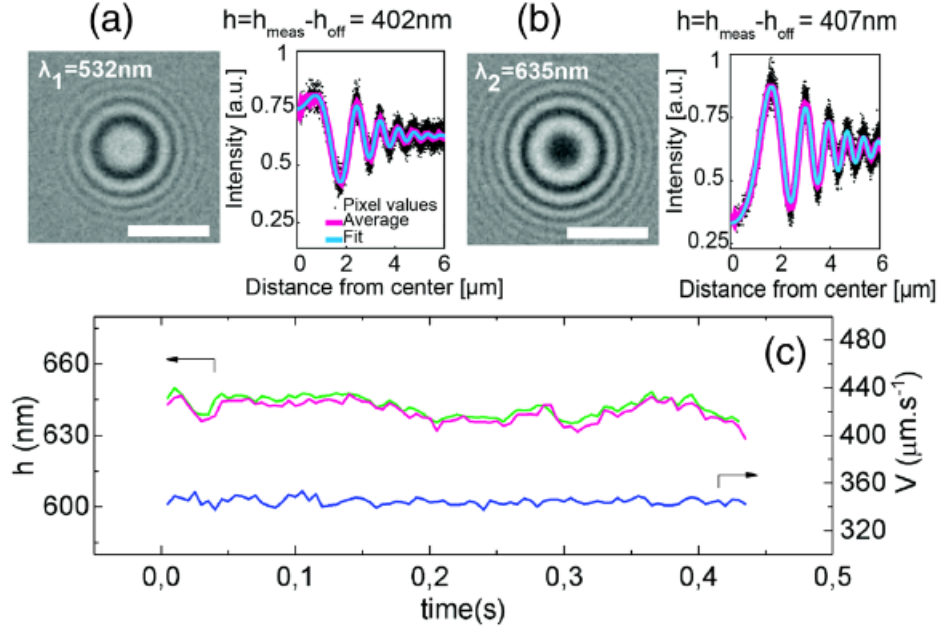


Figure 5: Figure from [36] representing RICHM with two wavelengths. (a) Left: interference patterns created with a wavelength $\lambda_1 = 532$ nm (scale bar $5 \mu\text{m}$). Right: radial intensity profile (black dots) extracted from the image, azimuthally averaged (magenta line) and fitted with Eq.3.2.8 to measure the height of the particle (here h). (b) Same as (a) with a wavelength $\lambda_2 = 635$ nm. (c) Time series of the height of a particle h (green: λ_1 , magenta: λ_2) and the particle velocity measured along the flow in blue.

interest at the mathematical description of this phenomenon. In the far field, we can describe two different one-dimensional electric field vectors of the same pulsation ω [44] as:

$$\vec{E}_1(\vec{r}, t) = \vec{E}_{01} \cos(\vec{k}_1 \cdot \vec{r} - \omega t + \epsilon_1) , \quad (3.2.1)$$

and

$$\vec{E}_2(\vec{r}, t) = \vec{E}_{02} \cos(\vec{k}_2 \cdot \vec{r} - \omega t + \epsilon_2) . \quad (3.2.2)$$

Where the k is the wave number $k = 2\pi n_m / \lambda$, λ denoting the illumination wavelength, n_m the optical index of the medium, $\epsilon_{1,2}$ the initial phase of each waves and \vec{r} the position from the source. Here, the origin ($\vec{r} = \vec{0}$) could be taken at the position of the first reflection (on the glass slide) thus at the particle, \vec{r} would be given by the particle's height such that $|\vec{r}| = z$ the particle-substrate distance. Experimentally, we measure the intensity of the interference patterns, those can be computed from the time averaged squared sum of the electric field $\vec{E} = \vec{E}_1 + \vec{E}_2$. The measured intensity is thus given by:

$$\begin{aligned}
I &= \langle \vec{E}^2 \rangle = \langle \vec{E}_1^2 + \vec{E}_2^2 + 2\vec{E}_1 \cdot \vec{E}_2 \rangle = \langle \vec{E}_1^2 \rangle + \langle \vec{E}_2^2 \rangle + 2\langle \vec{E}_1 \cdot \vec{E}_2 \rangle \\
&= \frac{E_{01}^2}{2} + \frac{E_{02}^2}{2} + 2\langle \vec{E}_1 \cdot \vec{E}_2 \rangle,
\end{aligned} \tag{3.2.3}$$

where $\langle \vec{E}_1 \rangle$ and $\langle \vec{E}_2 \rangle$ are respectively given by I_1 and I_2 , the incident light intensities. Using the trigonometric formula $2 \cos(a) \cos(b) = \cos(a+b) \cos(a-b)$ we have:

$$\langle \vec{E}_1 \cdot \vec{E}_2 \rangle = \left\langle \frac{1}{2} \vec{E}_{01} \vec{E}_{02} \left[\cos(\vec{k}_1 \cdot \vec{r} - \vec{k}_2 \cdot \vec{r} + \phi) + \cos(2\omega t + \phi') \right] \right\rangle. \tag{3.2.4}$$

As we average over the time, the second cos will vanish since in general $\langle \cos(at+b) \rangle_t = 0$ thus:

$$\langle \vec{E}_1 \cdot \vec{E}_2 \rangle = \frac{1}{2} \langle \vec{E}_{01} \vec{E}_{02} \rangle \cos(\vec{k}_1 \cdot \vec{r} - \vec{k}_2 \cdot \vec{r} + \phi) \tag{3.2.5}$$

with ϕ the phase difference between the two fields, which is generally equal to π due to the reflection properties on a higher index. Indeed a colloid has generally a greater optical index than the dilution medium. finally, the total intensity can be read as:

$$I = I_1 + I_2 + 2\sqrt{I_1 I_2} \cos(\vec{k}_1 \cdot \vec{r} - \vec{k}_2 \cdot \vec{r} + \phi) \tag{3.2.6}$$

By taking $k_1 = -k_2$ due to the reflection properties, we have:

$$I = I_1 + I_2 + 2\sqrt{I_1 I_2} \cos\left(\frac{4\pi n_m}{\lambda} z + \phi\right) \tag{3.2.7}$$

If we now suppose that we have a spherical particle at a height z we can develop the radial interference intensity $I(x)$ as [43]:

$$I(x) = A_0 + A_1 e^{-b_1 x^2} + A_2 e^{-b_2 x^2} \cos\left[\frac{4\pi n_m}{\lambda} (g(x) + z) + \phi\right] \tag{3.2.8}$$

Where A_i and b_i are fit parameters and $g(x)$ donotes the contour of the sphere. Finally, this method is great because the equation are computationally light and permits to have a quick tracking of particles. However, as we can see on Eq.3.2.8, due to the periodicity

of the cosinus, the interference pattern will be the same for all heights z separated by a distance $\lambda/2n_m \approx 200$ nm (for $\lambda = 532$ nm and $n_m = 1.33$). It is possible to extend this limitation by using 2 different wavelengths to ≈ 1.2 μm as used in [36]. Despite the precision of this method which can reach the 10 nm spatial resolution on the particle position measurement, the range limitation is not compatible with the study of < 5 μm particle's Brownian motion making RICH not usable for our context since we need at minimum a 5 μm of spatial extension on the height measurement.

3.2.2 Lorenz-Mie Fit

A way hologram, is to look at the superimposition of the scattered field \vec{E}_s and incident field \vec{E}_0 . This way, we could track and characterize even small particles. This method has been developed in the early 2000 [45, 46]. Since, a lot of studies has been realised with this method.

Let's the incident field be a plane wave uniformly polarized along the axis \hat{e} , with an amplitude E_0 and propagating along the z direction :

$$\vec{E}_0(\vec{r}, z) = E_0(\vec{r})e^{ikz}\hat{e} \quad (3.2.9)$$

Let's consider a particle of radius a at a position \vec{r}_p , the scattered field can be written using the Lorenz-Mie theory [44] as:

$$\vec{E}_s(\vec{r}) = \vec{f}_s(k(\vec{r} - \vec{r}_p))E_0(\vec{r})\exp(-ikz) \quad (3.2.10)$$

With \vec{f}_s the Lorenz-Mie scattering function [44]. The intensity I that we measure at \vec{r} is given by the super imposition of incident and scattered waves. Since the measurements are done at the focal plane, I is given by:

$$\begin{aligned} I(\vec{r}) &= |\vec{E}_s(\vec{r}, 0) + \vec{E}_0(\vec{r}, 0)|^2 \\ &= E_0^2(\vec{r}) + 2E_0^2 \operatorname{Re} \left(\vec{f}_s(k(\vec{r} - \vec{r}_p))\hat{e} \right) + |\vec{f}_s(k(\vec{r} - \vec{r}_p))|^2 \end{aligned} \quad (3.2.11)$$

The most of the experimental defects on the images are due to spacial illumination variation caused by dust particle and such. It can be corrected by normalizing the image by the background. In another word, we normalize $I(\vec{r})$ by the intensity of the incident field

$I_0 = E_0(\vec{r})^2$ which is the experimental background. It can be measured by different methods, one is to have an empty field of view and the other one, which is more convenient is to take the median of a stack of images. Naturally, for having the later to work, the movie should be long enough to have the particle diffuse enough, if not a ghost of the particle will appear on the background. This process also permits to get rid of the immobile particle that could generate any additional noise. An example of an hologram before and after the normalization is shown in Fig.6 a-c). We write the normalized intensity I/I_0 :

$$\frac{I(\vec{r})}{I_0} = 1 + 2 \operatorname{Re} \left(\vec{f}_s(k(\vec{r} - \vec{r}_p)) \hat{e} \right) + |\vec{f}_s(k(\vec{r} - \vec{r}_p))|^2 \quad (3.2.12)$$

Now that we have the analytical form of the holograms intensity it is possible to fit an experimental one to Eq.3.2.12 as shown in Fig.6 d-e). For the sake of completeness I will detail the Lorenz-Mie scattering function, $\vec{f}_s(k\vec{r})$, it is given by the series:

$$\vec{f}_s(k\vec{r}) = \sum_{n=1}^{n_c} \frac{i^n(2n+1)}{n(n+1)} \left(i a_n \vec{N}_{eln}^{(3)}(k\vec{r}) - b_n \vec{M}_{oln}^{(3)}(k\vec{r}) \right) \quad (3.2.13)$$

where $\vec{N}_{eln}^{(3)}(k\vec{r})$ and $\vec{M}_{oln}^{(3)}(k\vec{r})$ are the vector spherical harmonics. a_n and b_n are some coefficients that depend on the particle properties and illumination properties. For a spherical and isotropic particle of radius a and refractive index n_p which is illuminated by a linearly polarized plane wave, the a_n and b_n coefficients are expressed in terms of spherical Bessel j_n and Hankel h_n functions as [44]:

$$a_n = \frac{\zeta^2 j_n(\zeta ka) k a j'_n(ka) - j_n(ka) [\zeta k a j_n(\zeta ka)]'}{\zeta^2 j_n(\zeta ka) k a h_n^{(1)'}(ka) - h_n^{(1)}(ka) \zeta k a j'_n(\zeta ka)} \quad (3.2.14)$$

and

$$b_n = \frac{j_n(\zeta ka) k a j'_n(ka) - j_n(ka) \zeta k a j'_n(mka)}{j_n(\zeta ka) k a h_n^{(1)'}(ka) - h_n^{(1)}(ka) \zeta k a j'_n(mka)}, \quad (3.2.15)$$

where $\zeta = n_p/n_m$ and the prime notation denotes differentiation with respect to the argument. As we can see, the holograms given by Eq.3.2.13 will vary with a lot of parameters (λ , n_m , n_p , a and \vec{r}_p) which can all be fitted. In general, the illumination wavelength λ and medium index n_m are known and do not need to be fitted. From only one hologram it is thus possible to measure precisely the position of the particle \vec{r}_p and in

the same time characterize the radius and optical index of the colloid. It is even possible to characterize a particle without a priori knowledge of its characteristics using Bayesian approach [47, 48].

Computing Eq.3.2.13 numerically brings another interesting question, as it is analytically written as a sum over n one could ask after which number of terms n_c the series will converge. It has actually been found that the series converge after a number of terms [49]

$$n_c = ka + 4.05(ka)^{1/3} + 2 . \quad (3.2.16)$$

Consequently, larger particles' holograms will need more terms to converge and, hence, are longer to fit. As an example, the largest particles used during my thesis have a radius $a = 2.5 \mu\text{m}$ leading to a number of terms $n_c = 55$ in water and $\lambda = 532 \text{ nm}$, for the smallest ones, where $a = 0.5 \mu\text{m}$ we find $n_c = 18$ which makes a huge difference in practice.

Finally, Lorenz-Mie is the most versatile in-line holographic method as it permits to track and characterize unique particles even without a priori knowledge. Besides, writing the Lorenz-Mie function \vec{f}_s for particular cases such as anisotropic [50] or non-spherical particles [51] and also in the case of particle clusters [50, 52]. Additionally, it can reach really high precision as the tenth of nanometer on the position and radius and 10^{-3} on the optical index [46]. Unfortunately, the Lorenz-Mie fitting suffer from a major drawback which is the time needed to fit one image. For example, a 200 by 200 pixels image of a $2.5 \mu\text{m}$ particle's hologram can take up to two minutes to be fitted using a pure and straightforward python algorithm. A lot of work has been done to have faster tracking such as random-subset fitting [53], GPU (graphical processing unit) acceleration, machine-learning [54, 55] and deep neural networks [56].

3.2.3 Rayleigh-Sommerfeld back-propagation

Rayleigh-Sommerfeld back-propagation [58] works on the same principle as the Lorenz-Mie fitting but assumes that we have small scatterers.

$$|\zeta - 1| \ll 1 \text{ and } ka|\zeta - 1| \ll 1 . \quad (3.2.17)$$

In this case, at the focal plane, the intensity of the scattered field is smaller than the incident field. Additionally, the term $|\vec{E}_s|^2$ can be ignored. Thus, the normalized intensity,

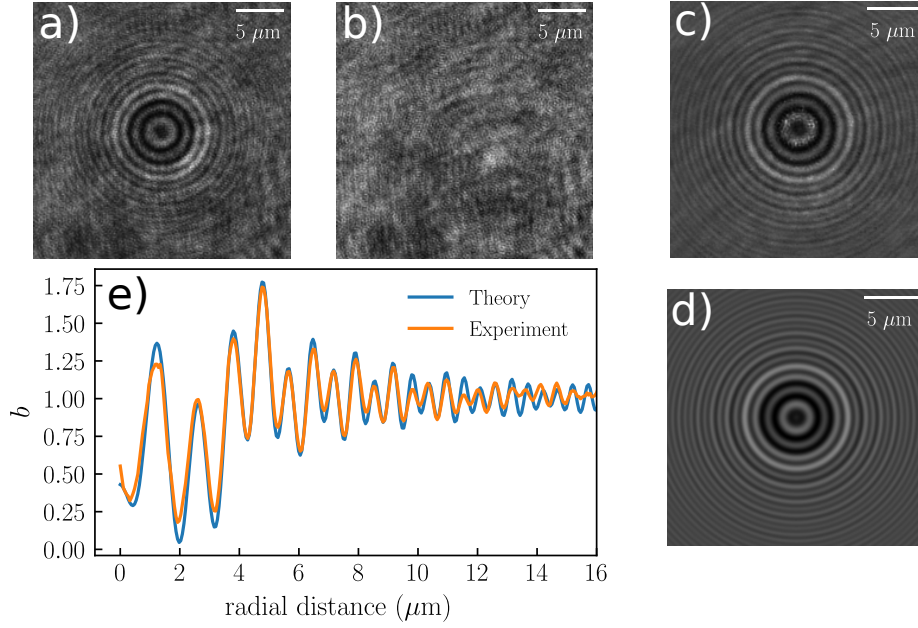


Figure 6: a) Raw hologram of a $2.5 \mu\text{m}$ polystyrene particle measured experimentally with the setup detailed in the chapter 3.3. b) Background obtained by taking the mean value of the time series of images of the diffusing particle. c) Normalized hologram given by dividing a) by b). d) Result of the fit of c) using Eq.3.2.12 the particle is found to be at a height $z = 14.77 \mu\text{m}$. e) Comparison of the normalized radial intensity, obtained experimentally from c) and theoretically from d).

Eq.3.2.12 can be rewritten as:

$$b(\vec{r}) = 1 + 2 \operatorname{Re} \left(\frac{E_s(\vec{r}, 0)}{E_0(\vec{r})} \right) . \quad (3.2.18)$$

If you can retrieve completely the scattered field from an image it is possible to reconstruct it above the focal plane by convolution using the Rayleigh-Sommerfeld propagator [59]:

$$h_{-z}(\vec{r}) = \frac{1}{2\pi} \frac{\partial}{\partial z} \frac{e^{ikR}}{R} , \quad (3.2.19)$$

where $R^2 = r^2 + z^2$ and the sign convention on the propagator indicates if the particle is below or above the focal plane. Using this propagator we have:

$$E_s(\vec{r}, z) = E_z(\vec{r}, 0) \otimes h_{-z}(\vec{r}) \quad (3.2.20)$$

Using the convolution theorem [57, 59–61] we can write the reconstructed scattered field at a height z by supposing a uniform illumination as:

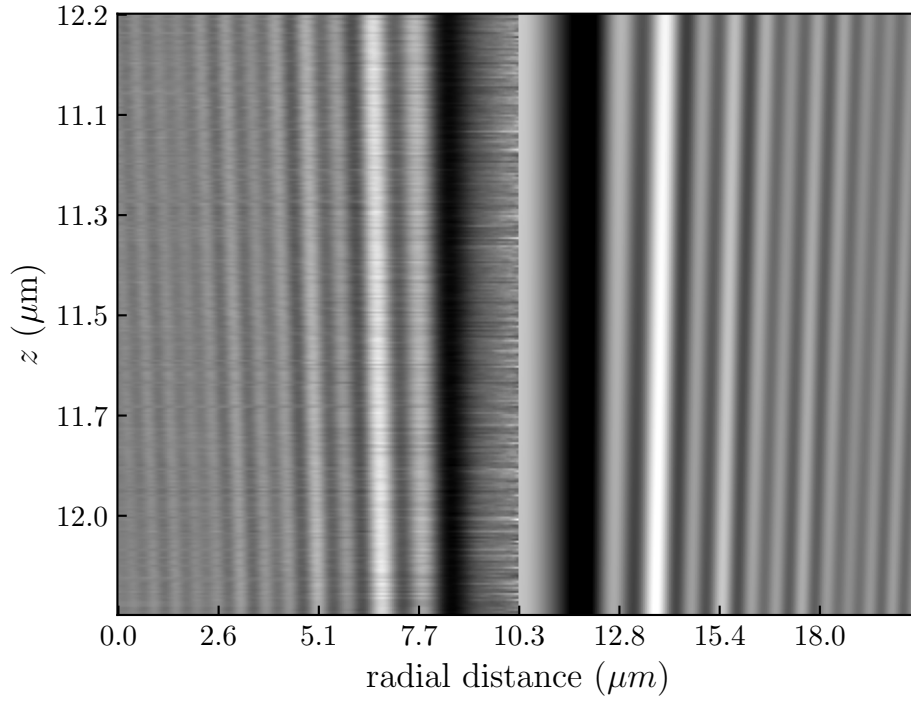


Figure 7: On the left, experimentally measured holograms' radial intensity stack. Generated from a polystyrene bead (Sigma Aldrich) of nominal radius $a = 1.5 \pm 0.035 \mu\text{m}$ using the experimental setup explained in chapter 3.3. The calibration of this particle radius and optical index is shown in Fig.11. On the right, the corresponding theoretical stack using the result of each individual hologram's fit.

$$E_s(\vec{r}, z) \approx \frac{e^{ikz}}{4\pi^2} \int_{-\infty}^{\infty} B(\vec{q}) H(\vec{q}, -z) e^{i\vec{q} \cdot \vec{r}} d^2q, \quad (3.2.21)$$

where $B(\vec{q})$ is the Fourier transform of $b(\vec{r})$ and $H(\vec{q}, -z)$ is given by

$$H(\vec{q}, -z) = e^{iz\sqrt{k^2 - q^2}}. \quad (3.2.22)$$

Finally, using Eq.3.2.21 we can reconstruct the scattered field and intensity since $I(\vec{r}) = |E_s(\vec{r})|^2$ as shown in Fig.8. Those equation are way less computational intensive than the Lorenz-Mie function Eq.3.2.13. Thus tracking can be way faster, moreover, Fourier transforms can be largely accelerated using GPU. Additionally, as the propagator Eq.3.2.19 take only into account the intensity of the image, this method does not require any information on the particle and number of particles, here, we just need to assume that we have spherical colloids. Thus this method is great to reconstruct the 3D position of a lot of particles or clusters formations. However, the major drawback is that it is the less precise of the presented measurements and that we can't use it to characterize the particles generating the holograms.

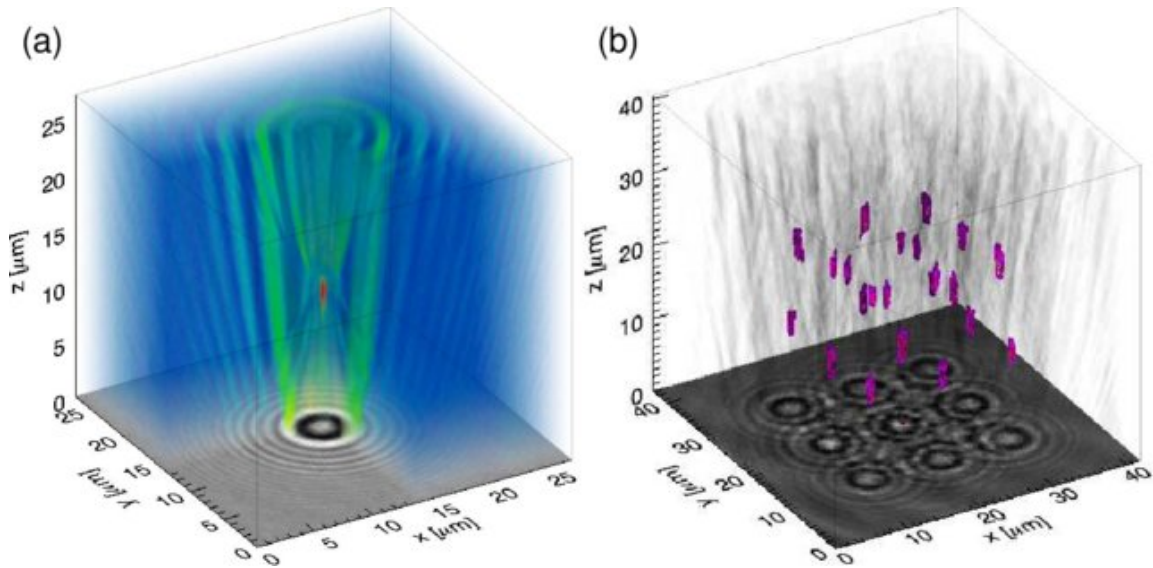


Figure 8: Figure from [57] a) Volumetric reconstruction using Eq.3.2.21 of the scattered intensity due to a single colloidal sphere, colored by intensity. b) Volumetric reconstructions of 22 individual $1.58 \mu\text{m}$ diameter silica spheres organised in bcc lattice using holographic optical tweezers in distilled water. Colored regions indicate the isosurface of the brightest 1 percent of reconstructed voxels.

3.2.4 Conclusion

Finally, the method we choosed is the Lorenz-Mie fitting method, since this method permits the characterization of single particle. Indeed, since we are interested to fine effects near the surface we need to know perfectly the radius of the particle we have recorded. This feature also make our all process, calibration free as we don't need to assume any physical properties. In the following the experimental setup is going to be detailed .

3.3 Experimental setup

In order to observe the holograms we use an home made inversed microscope as shown on the Fig.9 and shematized in Fig.10. A sample consists of a parallelepipedic chamber ($1.5 \text{ cm} \times 1.5 \text{ cm} \times 150 \mu\text{m}$), made from two glass covers, a parafilm spacer, and sealed with vacuum grease, containing a dilute suspension of spherical polystyrene beads. We used 3 differents sizes, of nominal raddi $0.56 \mu\text{m}$, $1.5 \mu\text{m}$ and $2.5 \mu\text{m}$, at room temperature T , in distilled water (type 1, MilliQ device) of viscosity $\eta = 1 \text{ mPa.s}$. The sample is illuminated by a collimated laser beam with a $521 \mu\text{m}$ wavelength. The explain in the chapter 3.3..., the light scattered by one colloidal particle at a given time t interferes with the incident beam. An oil-immersion objective lens (x60 magnification, 1.30 numerical aperture) collects the ersulting instantaneous interference pattern, and relays it to a camera (Basler acA1920-155um) with a 51.6 nm/pixel resolution (see Fig.6a)). The exposure time of the camera is set to 3 ms to avoid motion-induced blurring of the image, as a general rule, the particle should not diffuse more than the pixel size during that time.

3.4 Hologram fitting strategy

3.4.1 How to fasten the process ?

As presented in the section 3.2.2 about the Lorenz-Mie fitting. The main drawback is the time to fit an image, from 30 seconds for the images of 100×100 pixels to a few minutes for the 500×500 pixels. We can directly see a bottleneck, indeed, if we want to track one trajectory made of 100 000 images we would need to wait ≈ 70 days for a series of images that need only a few minutes to be shot experimentaly. When I started my PhD, two groups, the Grier's lab and the Manoharan's lab, had already introduced python packages, respectively, Pylorenzmie and Holopy in order to inverse holograms. They had

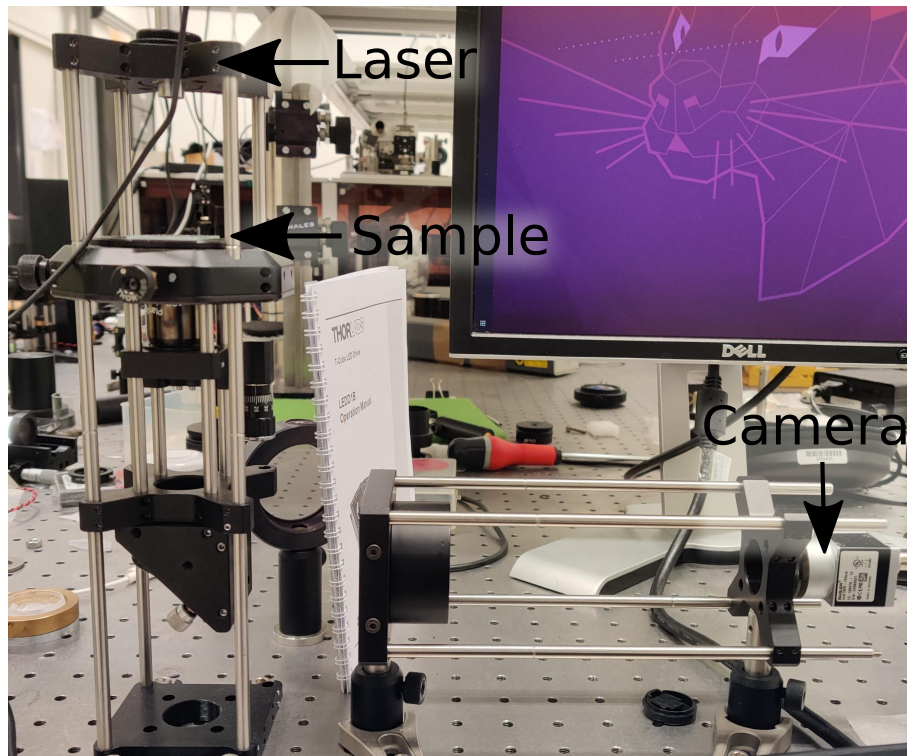


Figure 9: Photo of the custom build microscope used along my thesis. It is mainly composed of Thorlabs cage system. The camera used is a Basler acA1920-155um, we use a x60 magnification and 1.30 numerical aperture oil immersion objective and the laser is colimated and has a $521\mu\text{m}$ wavelength.

introduce ways to only fit a set of randomly choosen pixels and demonstrated that taking only 1% of the image pixel could lead to similar precision and improve considerably the fits [53]. Unfortunately, even if this is faster, it leads to a few images per second and still is too long for the amount of data we wanted to have. Ironically, this part of my project is certainly the one I spent the most time, and learn a lot of things on code optimization and computer cluster usage. It's around the half of my thesis that Pylorenzmie got a new commit on their github repository which was telling that they succeeded on using GPU acceleration using CUDA. This was not an easy task since they needed to reconstruct the Bessel, fortunatly it is possible by using continued fractions [49]. This tiny update permits to fit whole images at a whooping speed improvment of 20 fps. At this, speed we fit the tridimension position of the particle, the radius and optical index. To have a more reliable and fast tracking what we do is that we will fit with all free parameters the first 10 000 of a movie and determine the physical properties of the colloidal particle and then fit the whole movie with only the position as a free parameter.

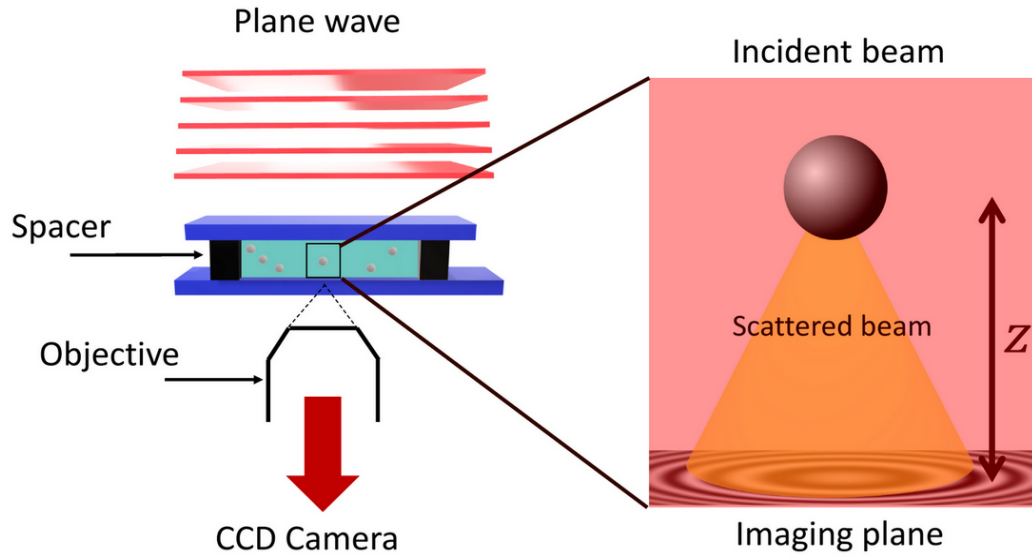


Figure 10: Schematic of the experimental setup. A laser plane wave of intensity E_0 illuminates the chamber containing a dilute suspension of microspheres in water. The light scattered by a particle interferes with the incident beam onto the focal plane of an objective lens, that magnifies the interference pattern and relays it to a camera.

3.4.2 Radius and optical index characterization

Once the data of the radius and optical index retrieved, the first quantity we can look at is the distribution of measurements. Using our 10 000 measurements we can plot the histograms of the measured a and n_p .

This simple histogram could suffice to measure the physical properties of the colloidal particle. However, we can go a bit further and look at the 2D histogram of the a and n_p as presented in the fig.XX here smoothed using a Gaussian kernel density estimator. As we can see it is not isotropic and it seems that the measurement of n_p and a are correlated.

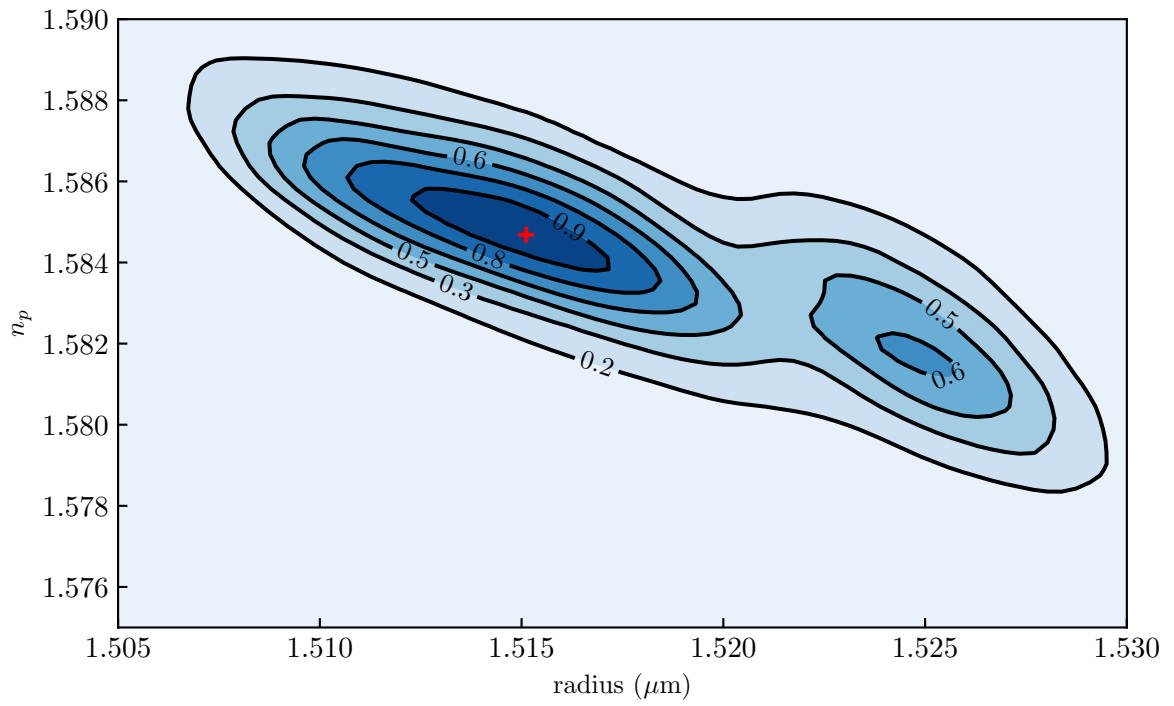


Figure 11: 2D Probability density function of the measurements of the optical index n_p and radius a . Black lines indicates iso-probability. Taking the 10% top probability, we measure $n_p = 1.585 \pm 0.002$ and $a = 1.514 \pm 0.003 \mu\text{m}$.

References

- [1] R. Baraniuk, D. Donoho, and M. Gavish, “The science of deep learning”, Proceedings of the National Academy of Sciences **117**, Publisher: National Academy of Sciences Section: Introduction, 30029–30032 (2020).
- [2] B. Lemieux, A. Aharoni, and M. Schena, “Overview of DNA chip technology”, Molecular Breeding **4**, 277–289 (1998).
- [3] Á. Ríos, M. Zougagh, and M. Avila, “Miniaturization through lab-on-a-chip: utopia or reality for routine laboratories? a review”, Analytica Chimica Acta **740**, 1–11 (2012).
- [4] A. Einstein, “Über die von der molekularkinetischen Theorie der Wärme geforderte Bewegung von in ruhenden Flüssigkeiten suspendierten Teilchen”, Annalen der Physik **vol. 4, t. 17** (1905).
- [5] J. Perrin, *Les Atomes*, Google-Books-ID: A0ltBQAAQBAJ (CNRS Editions, Nov. 14, 2014), 199 pp.
- [6] B. U. Felderhof, “Effect of the wall on the velocity autocorrelation function and long-time tail of brownian motion [†]”, The Journal of Physical Chemistry B **109**, 21406–21412 (2005).
- [7] M. V. Chubynsky and G. W. Slater, “Diffusing diffusivity: a model for anomalous, yet brownian, diffusion”, Physical Review Letters **113**, 098302 (2014).
- [8] A. V. Chechkin, F. Seno, R. Metzler, and I. M. Sokolov, “Brownian yet non-gaussian diffusion: from superstatistics to subordination of diffusing diffusivities”, Physical Review X **7**, 021002 (2017).
- [9] C. I. Bouzigues, P. Tabeling, and L. Bocquet, “Nanofluidics in the Debye Layer at Hydrophilic and Hydrophobic Surfaces”, Physical Review Letters **101**, Publisher: American Physical Society, 114503 (2008).
- [10] L. Joly, C. Ybert, and L. Bocquet, “Probing the Nanohydrodynamics at Liquid-Solid Interfaces Using Thermal Motion”, Physical Review Letters **96**, Publisher: American Physical Society, 046101 (2006).
- [11] J. Mo, A. Simha, and M. G. Raizen, “Brownian motion as a new probe of wettability”, The Journal of Chemical Physics **146**, Publisher: American Institute of Physics, 134707 (2017).

- [12] E. R. Dufresne, T. M. Squires, M. P. Brenner, and D. G. Grier, “Hydrodynamic Coupling of Two Brownian Spheres to a Planar Surface”, *Physical Review Letters* **85**, Publisher: American Physical Society, 3317–3320 (2000).
- [13] L. P. Faucheux and A. J. Libchaber, “Confined brownian motion”, *Physical Review E* **49**, 5158–5163 (1994).
- [14] E. R. Dufresne, D. Altman, and D. G. Grier, “Brownian dynamics of a sphere between parallel walls”, *EPL (Europhysics Letters)* **53**, Publisher: IOP Publishing, 264 (2001).
- [15] H. B. Eral, J. M. Oh, D. v. d. Ende, F. Mugele, and M. H. G. Duits, “Anisotropic and hindered diffusion of colloidal particles in a closed cylinder”, *Langmuir* **26**, Publisher: American Chemical Society, 16722–16729 (2010).
- [16] P. Sharma, S. Ghosh, and S. Bhattacharya, “A high-precision study of hindered diffusion near a wall”, *Applied Physics Letters* **97**, Publisher: American Institute of Physics, 104101 (2010).
- [17] J. Mo, A. Simha, and M. G. Raizen, “Broadband boundary effects on brownian motion”, *Physical Review E* **92**, 062106 (2015).
- [18] M. Matse, M. V. Chubynsky, and J. Bechhoefer, “Test of the diffusing-diffusivity mechanism using near-wall colloidal dynamics”, *Physical Review E* **96**, 042604 (2017).
- [19] D. C. Prieve, “Measurement of colloidal forces with TIRM”, *Advances in Colloid and Interface Science* **82**, 93–125 (1999).
- [20] A. Banerjee and K. Kihm, “Experimental verification of near-wall hindered diffusion for the Brownian motion of nanoparticles using evanescent wave microscopy”, *Physical review. E, Statistical, nonlinear, and soft matter physics* **72**, 042101 (2005).
- [21] S. Sainis, V. Germain, and E. Dufresne, “Statistics of Particle Trajectories at Short Time Intervals Reveal fN-Scale Colloidal Forces”, *Physical review letters* **99**, 018303 (2007).
- [22] G. Volpe, L. Helden, T. Brettschneider, J. Wehr, and C. Bechinger, “Influence of noise on force measurements”, *Physical Review Letters* **104**, 170602 (2010).
- [23] M. Li, O. Sentissi, S. Azzini, G. Schnoering, A. Canaguier-Durand, and C. Genet, “Subfemtonewton force fields measured with ergodic Brownian ensembles”, *Physical Review A* **100**, 063816 (2019).

- [24] S. K. Sainis, V. Germain, and E. R. Dufresne, “Statistics of particle trajectories at short time intervals reveal fN-scale colloidal forces”, *Physical Review Letters* **99**, 018303 (2007).
- [25] B. Robert, “XXVII. A brief account of microscopical observations made in the months of June, July and August 1827, on the particles contained in the pollen of plants; and on the general existence of active molecules in organic and inorganic bodies”, *The Philosophical Magazine* **4**, Taylor & Francis, 161–173 (1828).
- [26] S. Peter, “Brownian Motion”, **Brownian motion**.
- [27] J. Perrin, “Mouvement brownien et molécules”, *J. Phys. Theor. Appl.* **9**, 5–39 (1910).
- [28] A. Genthon, “The concept of velocity in the history of brownian motion”, *The European Physical Journal H* **45**, 49–105 (2020).
- [29] P. Langevin, “Sur la théorie du mouvement brownien”, *C. R. Acad. Sci. (Paris)* 146, 530–533 **65**, 1079–1081 (1908).
- [30] H. Faxen, “Fredholm integral equations of hydrodynamics of liquids I”, *Ark. Mat., Astron. Fys* **18**, 29–32 (1924).
- [31] J. N. Israelachvili, *Intermolecular and surface forces*, Google-Books-ID: MVbWB-hubrgIC (Academic Press, May 29, 2015), 706 pp.
- [32] C. Fabry and A. Pérot, “Théorie et application d’une nouvelle méthode de spectroscopie interférentielle.”, *Ann. Chim. Phys.*, 7 (1899).
- [33] A. Perot and C. Fabry, “On the Application of Interference Phenomena to the Solution of Various Problems of Spectroscopy and Metrology”, *The Astrophysical Journal* **9**, 87 (1899).
- [34] A. A. Michelson and E. W. Morley, “On the relative motion of the earth and the luminiferous ether”, *American Journal of Science* **s3-34**, Publisher: American Journal of Science Section: Extraterrestrial geology, 333–345 (1887).
- [35] LIGO Scientific Collaboration and Virgo Collaboration et al., “GW151226: Observation of Gravitational Waves from a 22-Solar-Mass Binary Black Hole Coalescence”, *Physical Review Letters* **116**, in collab. with B. P. Abbott, Publisher: American Physical Society, 241103 (2016).
- [36] H. S. Davies, D. Débarre, N. El Amri, C. Verdier, R. P. Richter, and L. Bureau, “Elastohydrodynamic lift at a soft wall”, *Physical Review Letters* **120**, 198001 (2018).

- [37] A. S. Curtis, “THE MECHANISM OF ADHESION OF CELLS TO GLASS. A STUDY BY INTERFERENCE REFLECTION MICROSCOPY”, *The Journal of Cell Biology* **20**, 199–215 (1964).
- [38] T. J. Filler and E. T. Peuker, “Reflection contrast microscopy (RCM): a forgotten technique?”, *The Journal of Pathology* **190**, 635–638 (2000).
- [39] P. A. Siver and J. Hinsch, “THE USE OF INTERFERENCE REFLECTION CONTRAST IN THE EXAMINATION OF DIATOM VALVES”, *Journal of Phycology* **36**, 616–620 (2000).
- [40] I. Weber, “[2] reflection interference contrast microscopy”, in *Methods in enzymology*, Vol. 361, Biophotonics, Part B (Academic Press, Jan. 1, 2003), pp. 34–47.
- [41] L. Limozin and K. Sengupta, “Quantitative reflection interference contrast microscopy (RICM) in soft matter and cell adhesion”, *Chemphyschem: A European Journal of Chemical Physics and Physical Chemistry* **10**, 2752–2768 (2009).
- [42] F. Nadal, A. Dazzi, F. Argoul, and B. Pouligny, “Probing the confined dynamics of a spherical colloid close to a surface by combined optical trapping and reflection interference contrast microscopy”, *Applied Physics Letters* **79**, 3887–3889 (2002).
- [43] J. Raedler and E. Sackmann, “On the measurement of weak repulsive and frictional colloidal forces by reflection interference contrast microscopy”, *Langmuir* **8**, 848–853 (1992).
- [44] C. F. Bohren and D. R. Huffman, *Absorption and Scattering of Light by Small Particles* (Wiley, Apr. 1998).
- [45] B. Ovryn and S. H. Izen, “Imaging of transparent spheres through a planar interface using a high-numerical-aperture optical microscope”, *JOSA A* **17**, Publisher: Optical Society of America, 1202–1213 (2000).
- [46] S.-H. Lee, Y. Roichman, G.-R. Yi, S.-H. Kim, S.-M. Yang, A. v. Blaaderen, P. v. Oostrum, and D. G. Grier, “Characterizing and tracking single colloidal particles with video holographic microscopy”, *Optics Express* **15**, Publisher: Optical Society of America, 18275–18282 (2007).
- [47] P. Gregory, *Bayesian logical data analysis for the physical sciences: a comparative approach with mathematica® support*, Google-Books-ID: idkLAQAAQBAJ (Cambridge University Press, Apr. 14, 2005), 496 pp.

- [48] T. G. Dimiduk and V. N. Manoharan, “Bayesian approach to analyzing holograms of colloidal particles”, *Optics Express* **24**, Publisher: Optical Society of America, 24045–24060 (2016).
- [49] W. J. Lentz, “Generating Bessel functions in Mie scattering calculations using continued fractions”, *Applied Optics* **15**, Publisher: Optical Society of America, 668–671 (1976).
- [50] J. Fung and V. N. Manoharan, “Holographic Measurements of Anisotropic Three-Dimensional Diffusion of Colloidal Clusters”, *Physical Review E* **88**, 020302 (2013).
- [51] A. Wang, T. G. Dimiduk, J. Fung, S. Razavi, I. Kretzschmar, K. Chaudhary, and V. N. Manoharan, “Using the discrete dipole approximation and holographic microscopy to measure rotational dynamics of non-spherical colloidal particles”, *Journal of Quantitative Spectroscopy and Radiative Transfer* **146**, 499–509 (2014).
- [52] R. W. Perry, G. Meng, T. G. Dimiduk, J. Fung, and V. N. Manoharan, “Real-space studies of the structure and dynamics of self-assembled colloidal clusters”, *Faraday Discussions* **159**, Publisher: The Royal Society of Chemistry, 211–234 (2013).
- [53] T. G. Dimiduk, R. W. Perry, J. Fung, and V. N. Manoharan, “Random-subset fitting of digital holograms for fast three-dimensional particle tracking”, *Applied Optics* **53**, G177 (2014).
- [54] A. Yevick, M. Hannel, and D. G. Grier, “Machine-learning approach to holographic particle characterization”, *Optics Express* **22**, 26884 (2014).
- [55] M. D. Hannel, A. Abdulali, M. O’Brien, and D. G. Grier, “Machine-learning techniques for fast and accurate feature localization in holograms of colloidal particles”, *Optics Express* **26**, Publisher: Optical Society of America, 15221–15231 (2018).
- [56] L. E. Altman and D. G. Grier, “CATCH: Characterizing and Tracking Colloids Holographically Using Deep Neural Networks”, *The Journal of Physical Chemistry B* **124**, Publisher: American Chemical Society, 1602–1610 (2020).
- [57] F. C. Cheong, B. J. Krishnatreya, and D. G. Grier, “Strategies for three-dimensional particle tracking with holographic video microscopy”, *Optics Express* **18**, Publisher: Optical Society of America, 13563–13573 (2010).
- [58] L. Wilson and R. Zhang, “3d localization of weak scatterers in digital holographic microscopy using rayleigh-sommerfeld back-propagation”, *Optics Express* **20**, 16735 (2012).

-
- [59] J. W. Goodman, *Introduction to fourier optics*, Google-Books-ID: ow5xs_Rtt9AC (Roberts and Company Publishers, 2005), 520 pp.
 - [60] G. C. Sherman, “Application of the Convolution Theorem to Rayleigh’s Integral Formulas”, *JOSA* **57**, Publisher: Optical Society of America, 546–547 (1967).
 - [61] U. Schnars and W. P. Jüptner, “Digital recording and reconstruction of holograms in hologram interferometry and shearography”, *Applied Optics* **33**, 4373–4377 (1994).